Scripta Materialia 178 (2020) 433–437

Contents lists available at ScienceDirect

Scripta Materialia

journal homepage: www.elsevier.com/locate/scriptamat

Formation mechanism of Tb-rich shell in grain boundary diffusion processed Nd–Fe–B sintered magnets

Tae-Hoon Kim[a], T.T. Sasaki[a], T. Koyama[b], Y. Fujikawa[c], M. Miwa[c], Y. Enokido[c], T. Ohkubo[a], K. Hono[a,*]

[a] Elements Strategy Initiative Centre for Magnetic Materials, National Institute for Materials Science, Tsukuba 305-0047, Japan
[b] Department of Materials Design Innovation Engineering, Nagoya University, Furo-cho, Chikusa-ku, Nagoya 464-8603, Japan
[c] Materials Development Center, TDK Corporation, 570-2 Matsugashita, Minamihadori, Narita 268-8588, Japan

ARTICLE INFO

Article history:
Received 11 November 2019
Revised 2 December 2019
Accepted 2 December 2019

Keywords:
Permanent magnet
Nd–Fe–B
Coercivity
Grain boundary diffusion
Rare earth

ABSTRACT

We propose a new mechanism for the formation of Tb-rich shell in the Nd–Fe–B sintered magnet that was subjected to the grain boundary diffusion (GBD) process using TbH_2. Tb-enriched liquid films form along grain boundaries during the GBD process, which migrate by chemically induced liquid film migration (CILFM) to form Tb-rich shells behind. As a result, the Tb-rich shell form asymmetrically along a grain boundary with an abrupt concentration change at a core/shell interface with a gradual decrease of Tb concentration toward a grain boundary. These microstructure features can be reproduced with phase-field simulations.

The partial substitution of Nd with Dy and/or Tb in the $Nd_2Fe_{14}B$ phase leads to enhanced anisotropy field of the 2:14:1 phase, thereby increasing the anisotropy filed of the 2:14:1 phase, resulting in substantially improved coercivity of Nd–Fe–B based magnets [1]; however, the coercivity increase is accompanied by the loss of remanence because of the antiferromagnetic coupling between the heavy rare earth (HRE) elements and Fe in the 2:14:1 phase. To meet the demand to improve the coercivity with a minimum use of HRE and minimum reduction of remanence, HRE is selectively enriched along grain boundaries of sintered magnets through the so-cold grain boundary diffusion (GBD) process. There are various ways to supply HRE along grain boundaries, for example using sputtering [2–5], vapour deposition [3], dip coating with HRE in the form of pure metal [6], oxides and fluorides [7,8], or hydrides [9,10], electrophoretic deposition of fluorides [11], thin foils of HRE and eutectic alloys [12,13], eutectic alloy powders [14], blending Dy-rich powders [15]. The GBD process causes the formation of HRE-rich shell in 2:14:1 grains, which increases the local anisotropy field at the interface between Nd-rich grain boundary phase and 2:14:1 grains [16]. However, the upper limit for the coercivity ($\mu_0 H_c$) enhancement by the GBD process is limited to 2 T when HRE-free Nd–Fe–B sintered magnets is used as a starting material because the HRE-rich shell becomes thinner and its HRE concentration decreases as the depth from the magnet surface increases [5,6,9,10,12–14,16–20]. In order to obtain a clue to form a HRE-rich shell with a higher HRE concentration to the center of the GBD processed magnets, a number of investigations have been carried out for revealing the formation mechanism of the HRE-rich shell during the GBD process [16,18–23].

The formation of the Dy-rich shell in 2:14:1 grains by the GBD process has been attributed to the diffusion of Dy atoms from the Nd-rich grain boundary phases (GBPs) to the 2:14:1 phase [21]. However, the Dy diffusion alone cannot account for the shell formation because the Dy-rich shell commonly observed in the GBD processed magnets shows a unique microstructure that is difficult to explain by the solid diffusion of Dy, *i.e.*, an abrupt change of Dy concentration at faceted core/shell interfaces [6,20]. Oono et al. [19], Sepehri-Amin et al. [16], and Seelam et al. [20] reported that the surface of 2:14:1 grains partially melts during the Dy-vapor GBD process in equilibrium with a RE-rich liquid phase, and the Dy-rich shell is formed as a result of the solidification of the Dy-enriched liquid phase [16,19,20]. Although the solidification of the liquid phase can explain the faceted and compositionally abrupt core/shell interfaces [16,20], it cannot explain the asymmetric feature of the Dy-rich shell, *i.e.*, Dy-rich shell is formed asymmetrically along grain boundaries. Hence, the origin of the shell formation is still debatable. If only the

* Corresponding author.
E-mail address: kazuhiro.hono@nims.go.jp (K. Hono).

https://doi.org/10.1016/j.scriptamat.2019.12.002
1359-6462/

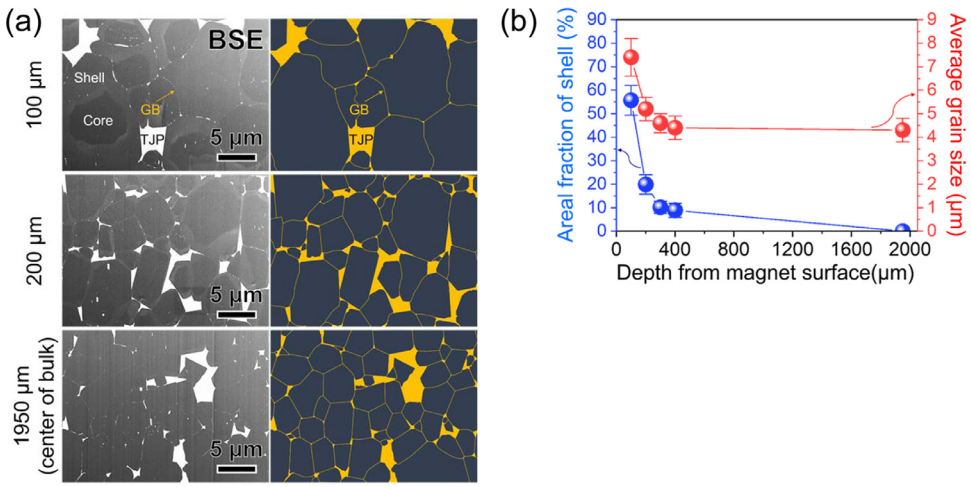

Fig. 1. (a) BSE images (left column) and schematic illustrations tracing grain boundaries and triple junction phases (right column) of GBD processed magnet observed at depths of 100, 200, and 1950 (centre of bulk) μm from the sample surface. (b) Variations in the areal fraction of Tb-rich shell (blue) and average grain size (red) against depth from the sample surface. (For interpretation of the references to colour in this figure legend, the reader is referred to the web version of this article.)

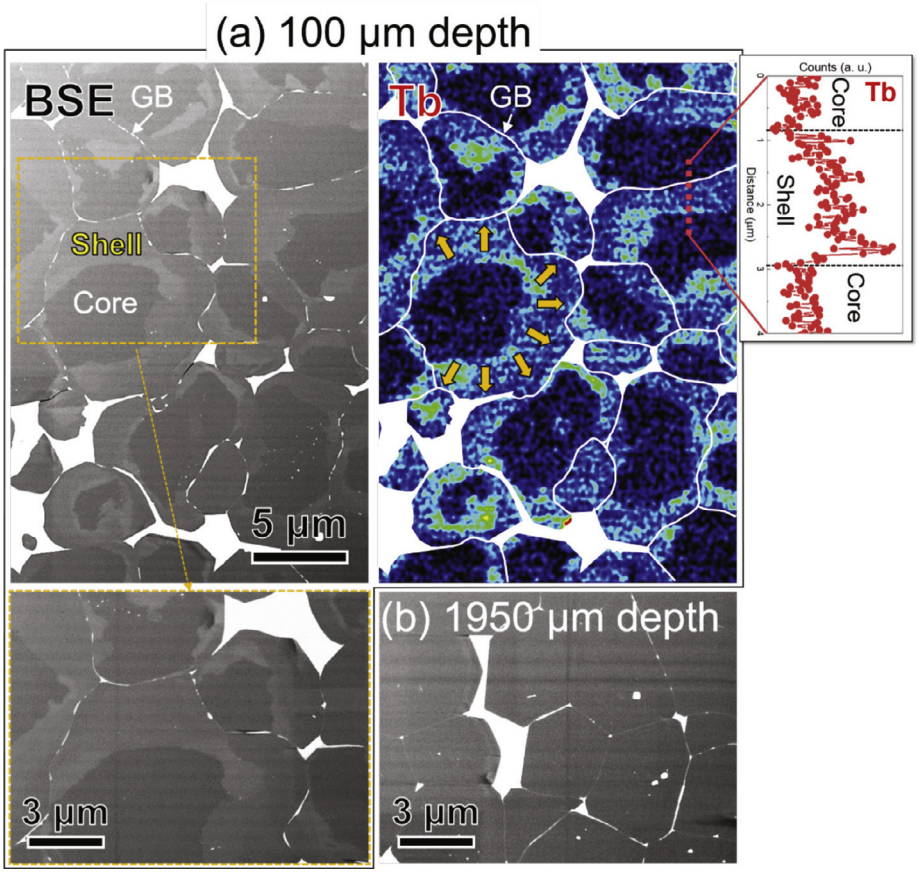

Fig. 2. (a) BSE image and EDS elemental map for Tb at a depth of 100 μm from the sample surface. The line scan profile of Tb across the shell (dashed line in Tb map) is shown in the inset of Fig. 2(a). The high magnification BSE image in the second row of Fig. 2(a) was taken from marked area (dashed rectangle) in the low magnification BSE image. For comparison, high-magnification BSE image taken at the centre part of the sample is shown in Fig. 2(b). The concentration profile measured by atom probe tomography across a grain boundary at the centre part is shown in Supplementary Fig. 1.

solidification of liquid is involved in the shell formation, a very thick Dy-rich shell observed near the surface of GBD processed magnets, in which the areal fraction of shell reaches ~50%, cannot be explained considering the liquid/solid phase equilibrium at the processing temperature of ~900 °C [20]. Hence, the aim of this study is to clarify the mechanism for the shell formation during the GBD process based on detailed microstructure investigations using (scanning) transmission electron microscopy ((S)TEM).

An as-sintered magnet with a nominal composition of Fe–30.5Nd–1.0B–0.8M (wt%) or $Fe_{79.05}Nd_{13.8}B_{6.0}M_{1.15}$ (in atomic ratio), where M = Cu, Co, Al, and Zr, was used as the starting material. 0.6 wt% TbH_2 powder was coated on the magnet surfaces

($17 \times 12 \times 3.9$ mm^3) parallel to the c-plane. The coated magnet was heat-treated at 970 °C for 12 h to permit the grain boundary diffusion (GBD) of Tb. Subsequently, the GBD processed sample was annealed at 520 °C. The magnetic properties of the samples were evaluated using a B-H tracer. After the GBD process, the coercivity of the magnet increased from 1.29 T to 1.89 T with a slight reduction of remanence (1.45 T → 1.40 T). Microstructure of the samples was analysed using scanning electron microscopy (SEM, Carl Zeiss Cross Beam 1540 EsB) and energy-dispersive X-ray spectrometry (EDS). The regions of interest were cleaned by focused ion beam (FIB, FEI Helios Nanolab 650) for SEM observation. Scanning transmission electron microscopy (STEM) observation was performed using a FEI Titan G^2 80–200 TEM with a probe aberration corrector. Thin foil specimens for the STEM observations were prepared by the lift-out technique using the FIB.

Fig. 1(a) shows back scattered electron (BSE) SEM images and schematic illustrations tracing the grain boundaries and triple junction phases (TJP) of the GBD processed magnet observed at depths of 100, 200, and 1950 µm from the surface of the sample. Since the thickness of the starting sample was 3.9 mm, the depth of 1950 µm corresponds to the centre of the sample. Tb-rich shells are imaged with bright grey contrast in the BSE images with darkly imaged core. The areal fraction of the Tb-rich shell decreases as the depth form the magnet surface increases from 100 µm to 1950 µm. It should be noted that the average grain size also decreases with increasing depth. Fig. 1(b) summarizes the variations in the average grain size and the areal fraction of the Tb-rich shell as a function of the depth from the magnet surface. Notably, the average grain size is correlated with the areal fraction of Tb-rich shell. At the depth of 1950 µm, where the Tb-rich shell formation is not visible in the SEM image, the average grain size is ~4.3 µm, the same as the grain size before being subjected to the GBD process. The 2:14:1 grains are coarsened to ~4.4, ~4.6, ~5.2, and ~7.4 µm as the areal fraction of Tb-rich shell increases to ~8.9 (400 µm depth), ~10.2 (300 µm depth), ~19.9 (200 µm depth), and ~55.7% (100 µm depth), respectively. In addition, the Nd-rich grain boundary appears to be pronouncedly bent as the areal fraction of Tb-rich shell increases, Fig. 1(a). These observations indicate that the formation of the Tb-rich shell is accompanied by grain coarsening.

Fig. 2(a) shows the SEM BSE images, EDS elemental map and line concentration profile for Tb at the depth of 100 µm from the surface of the sample. For comparison, the BSE image taken at the depth of 1950 µm is also shown in Fig. 2(b). As described in Fig. 1, the growth of the 2:14:1 grain accompanied by the bending of grain boundaries is clearly observed in the region where the thick Tb-rich shell is formed. As shown in the map and the line profile of Tb in Fig. 2(a), most of the Tb-rich shell is formed asymmetrically from grain boundaries, and the Tb concentration abruptly increases at the faceted core/shell interface. The Tb-concentration decreases gradually from the core/shell interface to the grain boundary at which Tb concentration shows a spike. The Tb-rich shell seems to grow from the core/shell interface to the outer region of the 2:14:1 grain, as illustrated by arrows in the Tb map of Fig. 2(a). This implies that the formation of the Tb-rich shell is accompanied by a grain boundary migration, resulting in the coarsening of the 2:14:1 grains with the formation of the curved grain boundaries as shown in Figs. 1 and 2. Although the Tb-rich shell is not observed at the centre of the magnet by the SEM image as shown in Fig. 2(b), Tb is enriched in the grain boundary phase and its concentration decrease from the GB phase/$Nd_2Fe_{14}B$ interface to the interior of the magnet within ~10 nm in depth as shown in the concentration profiles measured by atom probe tomography (Supplementary Fig. 2(b)), suggesting that solid diffusion of Tb occurred from the GB phase to the $Nd_2Fe_{14}B$ grain. Note that the peak position of Tb concentration slightly shift to the left side from the centre of the GB phase, suggesting the formation of a thin Tb-rich shell in the left side of the GB phase.

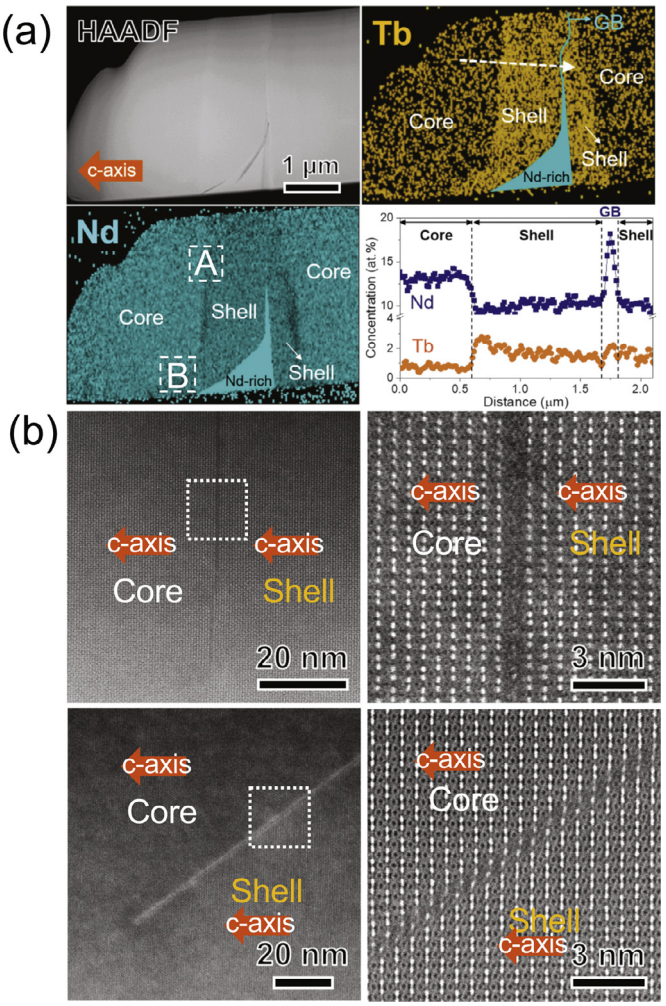

Fig. 3. (a) High angle annular dark field (HAADF)-STEM image and EDS elemental maps for Tb and Nd of a thick Tb-rich shell at a depth of 100 µm. The line concentration profiles for Tb and Nd were analysed across the core/shell interface along the dashed line in the Tb map. (b) HAADF-STEM images of planar defects in 2:14:1 crystal at core/shell interfaces. Note that images in A and B were taken from the region denoted as A and B in the Nd map of (a).

Note that a very similar grain boundary migration phenomenon involving a shell formation was reported by Kang et al. in the liquid phase sintered $Mo_{90}Ni_{10}$ alloy (wt%) that was subject to GBD process with W [24]. A thick W-enriched shell (~40 µm) having a faceted and compositionally abrupt core/shell interface was reported. Since thin liquid film is formed along grain boundaries, this unusual grain boundary migration phenomenon was termed the chemically-induced liquid film migration (CILFM) [24–26]. The coarsening of grains accompanied by curving of grain boundaries, the asymmetric formation of shell along the grain boundaries, and the higher concentration of diffusion source at the core/shell interface observed in the GBD processed Nd–Fe–B sintered magnets, shown in Figs. 1 and 2, have the same feature as CILFM observed in liquid sintered MoNi alloys [24–26]. Therefore, we conclude that the mechanism for the formation of Tb-rich shell in the Tb-GBD processed magnet is CILFM rather than the lattice diffusion of Tb [27] nor the solidification of the liquid phase after GBDP [16,19,20].

Partial melting of 2:14:1 grains occurs during the GBD process because the GBD process temperature (970 °C) is higher than the eutectic temperature of Nd/$Nd_2Fe_{14}B$ (685 °C) [20]. Fig. 3(a)

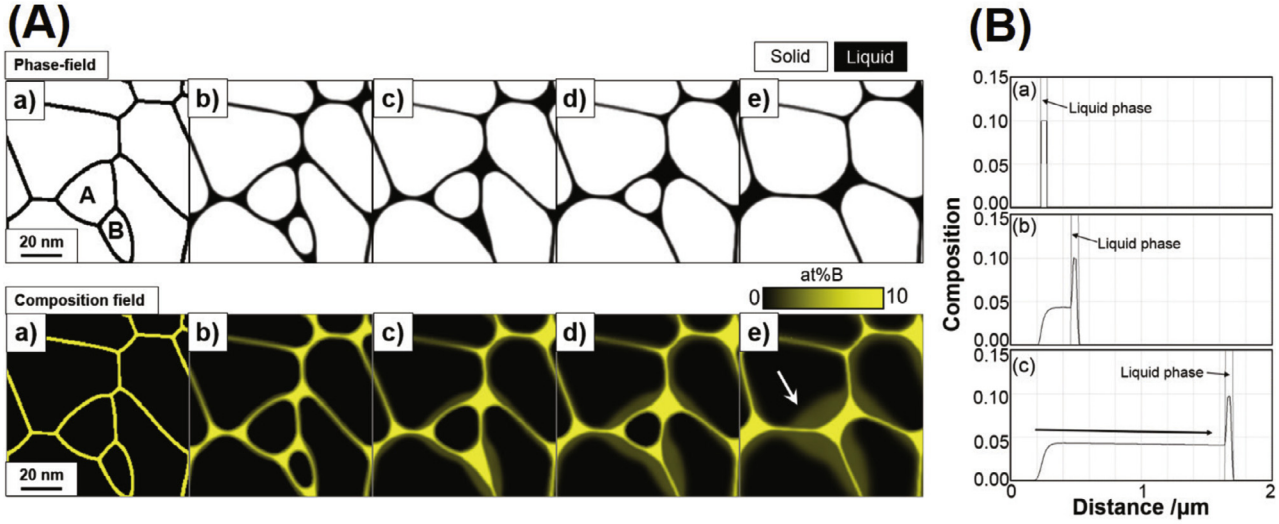

Fig. 4. (A) Two-dimensional phase-field simulation of the microstructure changes based on the CILFM mechanism during isothermal ageing for (a) t'=0, (b) t'=0.5, (c) t'=2.5, (d) t'=5 and (e) t'=10 (t' is dimensionless time). Upper row indicates the temporal evolution of the phase-field, where the white and black regions are solid phase and liquid phase, respectively. Lower row is the solute composition field where the local solute composition is represented by a brightness of yellow. See Supplementary Fig. 2 for movie. (B) One-dimensional phase-field simulation of the real scale calculation on the shell formation process during isothermal ageing for (a) t'=0, (b) t'=5 × 10^3 and (c) t'=3 × 10^4 (t' is dimensionless time). Solid line indicates the local composition of solute element, and the narrow region wedged between vertical thin solid line is a liquid phase. As a calculation condition, the solute composition in liquid phase is slightly decreased during ageing, continuously. (For interpretation of the references to colour in this figure, the reader is referred to the web version of this article.)

shows a high angle annular dark field (HAADF)-STEM image and the EDS elemental maps for Tb and Nd of the thick Tb-rich shell at the depth of 100 μm. The line concentration profiles for Tb and Nd were analysed across the core/shell interface along the dashed line in the Tb map. The abrupt change in the Tb and Nd concentration at the faceted core/shell interface is clearly observed. The Tb concentration within the shell gradually decreases with increasing the distance from the core/shell interface to the grain boundary phase. Fig. 3(b) shows the HAADF-STEM images taken from the core/shell interfaces denoted as A and B in the Nd map of Fig. 3(a). In region A, the (001) trace of the stacking fault is observed within the 2:14:1 crystal. While the brightly imaged Nd-rich layer is periodically observed in the atomic resolution HAADF image taken from the interior of core, a Nd-rich layer is missing along the core/shell interface. The presence of the stacking fault at the core/shell interface indicates a grain boundary was originally present at the core/shell interface, which migrated to the observed position by the chemically-induced liquid film migration (CILFM). Since the 2:14:1 phase was terminated at the grain boundary, solidification might have started from a wrong plane, resulting in the formation of a stacking fault. The planer defect observed in the region B is also a stacking fault introduced at the solid/liquid interface upon the solidification of the liquid phase with a different plane. The chemical composition in the solidified solid would take over that of the liquid film, and the gradual decrease of Tb concentration from the core/shell interface to a grain boundary indicates that the Tb concentration in the liquid film gradually decreases.

Oono et al. [19], Sephehri-Amin et al. [16], and Seelam et al. [20] proposed that the HRE-rich shell is formed by the solidification of the liquid phase during cooling from the temperature for GBD process. However, it cannot explain the formation of a very thick shell with the thicknesses of about 1–4 μm that is commonly observed in HRE-GBD processed sintered magnets (Figs. 1 and 2) [5,6,9,10,12–14,16–20]. In order to form such thick shells, a large fraction of the 2:14:1 phase must melt during the GBD process at 900–970 °C; however, it is unlikely considering the phase equilibrium at the processing temperature [20]. In order to understand how the HRE-rich shell form during the GBD process, we carried out two-dimensional phase-field simulation as shown in Fig. 4. Upper row indicates the temporal evolution of the phase-field, where the white and black regions are solid phase and liquid one, respectively. Lower row is the solute composition field, where the local solute concentration is represented by the brightness of the yellow colour. Unfortunately, the materials parameters of the Tb–Nd–Fe–B system such as the Gibbs energy, interfacial energy, diffusion coefficients are unknown, so this simulation is qualitative, *i.e.*, we employed the conventional multi-phase-field model [28], where we considered the liquid phase-field, polycrystalline solid phase-field, and local composition field of a hypothetical binary A-B alloy system. In order to reproduce the experimental microstructure changes, the grain growth simulation with a fixed volume fraction of a liquid phase is carried out, in which the solute content in liquid phase is fixed as A-10at%B because the solute element (Tb) is provided from outside continuously during the GBD process. Since the equilibrium composition of solid phase is assumed to be A-3at%B and the initial composition of solid phase is set as A-0at%B in the simulation, the solute-rich shell region appears behind the grain growth by CILFM (see the arrow in Fig. 4(A) e)). It is interesting that the solute-rich shells are formed when the small grains vanish during grain coarsening process (see the development of grains A and B in Fig. 4(A) a)). The real scale calculation on the shell formation process was carried out based on the one-dimensional phase-field simulation of composition profile in solute-rich shell as shown in the right column in Fig. 4, where we assumed the solute composition in liquid phase is slightly decreased continuously with time as the supply of the solute is not infinite. Note that the solute composition in the shell region decreases gradually due to the quite small change of solute concentration in the liquid film (see the arrow direction in Fig. 4(B) c)), which agrees with the experimental result in Fig. 3(a). Since the composition in the liquid phase at grain boundary region becomes Nd rich in real material as indicated in Fig. 3(a), the Tb concentration in liquid phase would decrease during the shell formation process. As shown in Fig. 1, CILFM causes coarsening of grains and the formation of unnecessarily-thick HRE-rich shell. Tb

can be enriched at GB phase/$Nd_2Fe_{14}B$ interfaces due to the solid-state diffusion of Tb from the GB phase to the interior of grains as observed by the APT data taken from the centre region of the magnet, Supplementary Fig. 2(b). Thus, the suppression of CILFM would be beneficial for designing high coercivity low HRE magnets.

In summary, we propose that the Tb-rich shell in the TbH_2-GBDP magnets is formed by the chemically induced liquid film migration (CILFM) based on the microstructure features observed by STEM/EDS analysis. Near the surface of the sample, significant grain coarsening was observed with curved grain boundaries. Thick Tb-rich shells (1–4 μm) were formed asymmetrically across original grain boundary. Tb concentration increase abruptly at the core/shell interface, and decreases gradually with the distance from the core/shell interface to grain boundaries. These microstructural characteristics can be reproduced with phase-field simulations assuming the presence of a liquid phase at grain boundaries. Stacking faults observed at the core/shell interface indicate that it was originally grain boundary before the Tb-rich shell was formed by chemically-induced liquid film migration (CILFM). Since Tb-rich shell form by CILFM even with a small fraction of the liquid phase, the presence of thick Tb-rich shells near the surface of the sample can also be explained. The CILFM should be the common mechanism for the formation of HRE-rich shell for both Tb and Dy GBD processes as liquid films are formed at grain boundaries regardless of the type of HRE elements.

Declaration of Competing Interest

The authors declare that they have no known competing financial interests or personal relationships that could have appeared to influence the work reported in this paper.

Acknowledgement

This work was in part supported by JST, Collaborative Research Based on Industrial Demand, Grant Number JPMJSK1618, and by Elements Strategy Initiative Centre for Magnetic Materials (ESICMM), Grant Number 12016013, through Ministry of Education, Culture, Sports, Science and Technology (MEXT).

Supplementary materials

Supplementary material associated with this article can be found, in the online version, at doi:10.1016/j.scriptamat.2019.12.002.

References

[1] M. Sagawa, S. Hirosawa, H. Yamamoto, S. Fujimura, Y. Matsuura, Jpn. J. Appl. Phys. 26 (1987) 785–800.
[2] K.T. Park, K. Hiraga, M. Sagawa, in: Proceedings of the 16th International Workshop on Rare Earth Magnets and their Applications, Japan Institute of Metals, 2000, pp. 257–264.
[3] K. Yoshimura, H. Morimoto, T. Odaka, Japan Patent, 4241890, 2008.
[4] N. Watanabe, M. Itakura, N. Kuwano, D. Li, S. Suzuki, K. Machida, Mater. Trans. 48 (2007) 915–918.
[5] D. Li, S. Suzuki, T. Kawasaki, K. Machida, Jpn. J. Appl. Phys. 47 (2008) 7876–7878.
[6] K. Loewe, C. Brombacher, M. Katter, O. Gutfleisch, Acta Mater. 83 (2015) 248–255.
[7] H. Nakamura, K. Hirota, M. Shimao, T. Minowa, M. Honshima, IEEE Trans. Magn. 41 (2005) 3844–3846.
[8] K. Hirota, H. Nakamura, T. Minowa, M. Honshima, IEEE Trans. Magn. 42 (2006) 2909–2911.
[9] W.Q. Liu, C. Chang, M. Yue, J.S. Yang, D.T. Zhang, Y.Q. Liu, J.X. Zhang, X.F. Yi, J.W. Chen, J. Magn. 18 (2013) 400–404.
[10] J. Di, G. Ding, X. Tang, X. Yang, S. Guo, R. Chen, A. Yan, Scr. Mater. 155 (2018) 50–53.
[11] M. Soderžnik, K.Ž. Rožman, S. Kobe, P. McGuiness, Intermetallics 23 (2012) 158–162.
[12] K. Loewe, D. Benke, C. Kübel, T. Lienig, K.P. Skokov, O. Gutfleisch, Acta Mater. 124 (2017) 421–429.
[13] K. Lu, X. Bao, M. Tang, G. Chen, X. Mu, J. Li, X. Gao, Scr. Mater. 138 (2017) 83–87.
[14] N. Oono, M. Sagawa, R. Kasada, H. Matsui, A. Kimura, Mater. Sci. Forum 654–656 (2010) 2919–2922.
[15] T. Hidaka, C. Ishizaka, M. Hosako, in: Proceedings of the 21st Workshop on Rare-Earth Permanent Magnets and Their Applications, Bled, Slovenia, 2010, pp. 100–201.
[16] H. Sepehri-Amin, T. Ohkubo, K. Hono, Acta Mater. 61 (2013) 1982–1990.
[17] B. Wu, Q. Zhang, W. Li, X. Ding, L. Yang, A. Ghafar Wattoo, L. Zhang, S. Mao, Z. Song, J. Appl. Phys. 123 (2018) 245112.
[18] W. Li, Q. Zhang, Q. Zhu, S. Xiao, C. Xu, L. Yang, B. Zheng, S. Mao, Z. Song, Scr. Mater. 163 (2019) 40–43.
[19] N. Oono, M. Sagawa, R. Kasada, H. Matsui, A. Kimura, J. Magn. Magn. Mater. 323 (2011) 297–300.
[20] U.M.R. Seelam, T. Ohkubo, T. Abe, S. Hirosawa, K. Hono, J. Alloys Compd. 617 (2014) 884–892.
[21] T.-H. Kim, S.-R. Lee, S.J. Yun, S.H. Lim, H.-J. Kim, M.-W. Lee, T.-S. Jang, Acta Mater. 112 (2016) 59–66.
[22] B. Wu, X. Ding, Q. Zhang, L. Yang, B. Zheng, F. Hu, Z. Song, Scr. Mater. 148 (2018) 29–32.
[23] T.-H. Kim, T.T. Sasaki, T. Ohkubo, Y. Takada, A. Kato, Y. Kaneko, K. Hono, Acta Mater. 172 (2019) 139–149.
[24] Ho Kyu Kang, S. Hackney, D.N. Yoon, Acta Metall. 36 (1988) 695–699.
[25] D.N. Yoon, Annu. Rev. Mater. Sci. 19 (1989) 43–58.
[26] R.A. Fournelle, Mater. Sci. Eng. A 138 (1991) 133–145.
[27] T.-H. Kim, S.-R. Lee, H.-J. Kim, M.-W. Lee, T.-S. Jang, Acta Mater. 93 (2015) 95–104.
[28] I. Steinbach, Model. Simul. Mater. Sci. Eng. 17 (2009) 073001.